



THE UNIVERSITY *of* EDINBURGH

Edinburgh Research Explorer

Scattering of swell by currents

Citation for published version:

Wang, H, Villas Boas, AB, Young, WR & Vanneste, J 2023, 'Scattering of swell by currents', *Journal of Fluid Mechanics*, vol. 975, A1. <https://doi.org/10.1017/jfm.2023.686>

Digital Object Identifier (DOI):

[10.1017/jfm.2023.686](https://doi.org/10.1017/jfm.2023.686)

Link:

[Link to publication record in Edinburgh Research Explorer](#)

Document Version:

Peer reviewed version

Published In:

Journal of Fluid Mechanics

General rights

Copyright for the publications made accessible via the Edinburgh Research Explorer is retained by the author(s) and / or other copyright owners and it is a condition of accessing these publications that users recognise and abide by the legal requirements associated with these rights.

Take down policy

The University of Edinburgh has made every reasonable effort to ensure that Edinburgh Research Explorer content complies with UK legislation. If you believe that the public display of this file breaches copyright please contact openaccess@ed.ac.uk providing details, and we will remove access to the work immediately and investigate your claim.



Banner appropriate to article type will appear here in typeset article

1 Scattering of swell by currents

2 Han Wang¹†, Ana B. Villas Bôas², William R. Young³ and Jacques
3 Vanneste¹

4 ¹School of Mathematics and Maxwell Institute for Mathematical Sciences, University of
5 Edinburgh, EH9 3FD, UK

6 ²Department of Geophysics, Colorado School of Mines, Golden CO 80401, USA

7 ³Scripps Institution of Oceanography, University of California at San Diego, La Jolla CA
8 92093-0213, USA

9 (Received xx; revised xx; accepted xx)

10 The refraction of surface gravity waves by currents leads to spatial modulations
11 in the wave field and, in particular, in the significant wave height. We examine
12 this phenomenon in the case of waves scattered by a localised current feature,
13 assuming (i) the smallness of the ratio between current velocity and wave group
14 speed, and (ii) a swell-like, highly directional wave spectrum.

15 We apply matched asymptotics to the equation governing the conservation of
16 wave action in the four-dimensional position–wavenumber space. The resulting
17 explicit formulas show that the modulations in wave action and significant wave
18 height past the localised current are controlled by the vorticity of the current
19 integrated along the primary direction of the swell.

20 We assess the asymptotic predictions against numerical simulations using
21 WAVEWATCH III for a Gaussian vortex. We also consider vortex dipoles to
22 demonstrate the possibility of ‘vortex cloaking’ whereby certain currents have
23 (asymptotically) no impact on the significant wave height. We discuss the role
24 of the ratio of the two small parameters characterising assumptions (i) and (ii)
25 above and show that caustics are only significant for unrealistically large values
26 of this ratio, corresponding to unrealistically narrow directional spectra.

27 1. Introduction

28 Surface gravity waves (SGWs) play a key role in the exchanges of energy, mo-
29 mentum and gases between the ocean and the atmosphere (Villas Bôas & Pizzo
30 2021). SGWs are forced by the wind and modulated by ocean currents through
31 transport and refraction. Over the past few decades, several studies have explored
32 the effects of ocean currents on SGWs. Early theoretical work focusses on the
33 formation of freak waves and identifies refraction as a possible mechanism for the
34 generation of large amplitude waves (White & Fornberg 1998; Heller *et al.* 2008;
35 Dysthe *et al.* 2008).

36 Recent studies examine how meso- and submesoscale ocean variability, such
37 as fronts, filaments and vortices, induces a corresponding variability in wave

† Email address for correspondence: hannnwangus@gmail.com

38 amplitudes (Ardhuin *et al.* 2017; Romero *et al.* 2017, 2020; Villas Boas *et al.* 2020;
 39 Vrećica *et al.* 2022). These studies often characterise the wave amplitudes using
 40 the significant wave height H_s , defined as four times the standard deviation of
 41 the surface displacement. They find that wave–current interactions at horizontal
 42 scales ranging from 10 to 200 km drive spatial gradients of H_s at similar scales.
 43 This indicates that air–sea fluxes might have spatial variability on these relatively
 44 small spatial scales.

45 One common approach to studying wave–current interactions is the use of ray
 46 tracing, often in its simplest form in which the kinematics of SGWs is tracked by
 47 solving the ray equations and ray density is used as a proxy for wave amplitude
 48 (e.g., Kenyon 1971; Mapp *et al.* 1985; Quilfen & Chapron 2019). While this simple
 49 form of ray tracing is a valuable tool for understanding wave refraction, it does
 50 not provide an accurate quantification of changes in wave amplitude, in particular
 51 changes in H_s . This quantification requires to solve the conservation equation for
 52 the density of wave action in the four-dimensional position–wavenumber phase
 53 space. This is challenging especially for the wave spectra of realistic sea states,
 54 distributed in both wavenumber and direction, instead of the pure plane waves
 55 that are often considered (see Heller *et al.* 2008, however). It is possible to solve
 56 the action equation numerically, albeit at great computational cost, either by
 57 discretising the phase space or by sampling its full four-dimensionality with a
 58 large ensemble of rays.

59 This paper proposes a complementary approach. It develops an asymptotic
 60 solution of the wave action equation, leading to explicit formulas for the changes
 61 in action and H_s induced by localised currents. Motivated by their ubiquity in the
 62 ocean, we focus on swell, that is, SGWs characterised by a spectrum that is narrow
 63 banded in both frequency (equivalently, wavenumber) and direction. We exploit
 64 the smallness of two parameters reflecting the narrowness of the spectrum and
 65 the weakness of the current relative to the wave speed. We approximate the wave
 66 action equation to leading order and solve it in closed form by integration along
 67 its characteristics (the approximate ray equations) by inspection. The formulas
 68 we obtain show that the changes in action and H_s depend on the currents through
 69 a ‘deflection function’ Δ given by the integral of the vorticity along the primary
 70 direction of wave propagation. We apply these formulas to simple flows – vortices
 71 and dipoles – and compare their predictions with the results of full integrations
 72 of the action conservation equation by a numerical wave model.

73 We formulate the problem, relate action and H_s , and introduce a model
 74 spectrum for swell in §2. We detail our scaling assumptions and carry out the
 75 (matched) asymptotics treatment of the wave action equation in §3. We compare
 76 asymptotic and numerical results for vortices and dipoles in §4. For vortices, we
 77 consider four different parameter combinations representative of ocean swell. We
 78 consider dipoles with axis along and perpendicular to the direction of the swell
 79 to demonstrate the possibility of a vanishing deflection function Δ , leading to
 80 asymptotically negligible changes in H_s , a phenomenon we refer to as ‘vortex
 81 cloaking’. In §5 we explore two limiting regimes of scattering: a linear regime,
 82 corresponding to weak currents and/or swell with relatively large angular spread,
 83 in which the changes in H_s are linear in the current velocity, and a caustic regime
 84 corresponding to strong currents and/or small angular spread. The caustic regime,
 85 in which the changes in H_s are large and concentrated along caustic curves, arises
 86 only for parameters values that are outside the range of typical ocean values. We

87 conclude with a summary of our findings and discuss prospects for future work
88 on the spatial variability of H_s in §6.

89 2. Formulation

90 We study the scattering problem sketched in figure 1. Deep-water SGWs, with
91 small initial directional spreading and a well defined peak frequency (swell)
92 impinge on a spatially compact coherent flow, such as an axisymmetric vortex or
93 a dipole.

94 2.1. Action conservation equation

95 In figure 1 we illustrate the scattering problem by tracing rays through an
96 axisymmetric vortex. We go beyond ray tracing, however, by using asymptotic
97 methods to obtain approximate analytic solutions of the conservation equation

$$98 \quad \partial_t \mathcal{A} + \nabla_{\mathbf{k}} \omega \cdot \nabla_{\mathbf{x}} \mathcal{A} - \nabla_{\mathbf{x}} \omega \cdot \nabla_{\mathbf{k}} \mathcal{A} = 0 \quad (2.1)$$

99 for the wave action density $\mathcal{A}(\mathbf{x}, \mathbf{k}, t)$ in the four-dimensional position–
100 wavenumber space (Komen *et al.* 1996; Janssen 2004). The action conservation
101 equation (2.1) relies on the WKB assumption of spatial scale separation between
102 waves and currents. In (2.1) $\omega(\mathbf{x}, \mathbf{k})$ is the absolute frequency of deep-water
103 SGWs

$$104 \quad \omega(\mathbf{x}, \mathbf{k}) = \sigma(k) + \mathbf{k} \cdot \mathbf{U}(\mathbf{x}). \quad (2.2)$$

105 We consider deep-water waves so that in (2.2) the intrinsic frequency is $\sigma(k) =$
106 \sqrt{gk} , with $k = |\mathbf{k}|$. The current velocity is taken to be horizontal and independent
107 of time and depth,

$$108 \quad \mathbf{U}(\mathbf{x}) = U(x, y) \hat{\mathbf{x}} + V(x, y) \hat{\mathbf{y}}. \quad (2.3)$$

109 The wave action equation (2.1) provides a phase-averaged description of the
110 scattering problem made possible by the scale separation between waves and cur-
111 rents. This places our work in contrast to that of Coste *et al.* (1999), Coste & Lund
112 (1999) and McIntyre (2019) who examined scattering without the simplification
113 afforded by scale separation and discuss phase effects such as the Aharonov–
114 Bohm effect. We also assume fixed currents and do not consider how these might
115 be modified by the presence of waves (see e.g. Humbert *et al.* 2017; McIntyre
116 2019).

117 2.2. Action spectrum and significant wave height

118 Denoting the sea-surface vertical displacement by $\zeta(\mathbf{x}, t)$, with root mean square
119 ζ_{rms} , and following Komen *et al.* (1996), we introduce a spectrum $\mathcal{F}(\mathbf{k}, \mathbf{x}, t)$ such
120 that

$$121 \quad \zeta_{rms}^2(\mathbf{x}, t) = \int \mathcal{F}(\mathbf{k}, \mathbf{x}, t) d\mathbf{k}. \quad (2.4)$$

122 Later we use a polar coordinate system (k, θ) in \mathbf{k} -space so that in (2.4) $d\mathbf{k} =$
123 $k dk d\theta$. The kinetic and potential energy densities for deep-water SGWs are
124 equipartitioned so that the energy spectrum is $g\mathcal{F}$ and the action spectrum,
125 $\mathcal{A}(\mathbf{x}, \mathbf{k}, t)$ in (2.1), is $\mathcal{A} = g\mathcal{F}/\sigma$. The significant wave height, $4\zeta_{rms}$ (Komen *et al.*
126 1996), is therefore

$$127 \quad H_s(\mathbf{x}, t) = \left(\frac{16}{g} \int \mathcal{A}(\mathbf{k}, \mathbf{x}, t) \sigma(k) d\mathbf{k} \right)^{1/2}. \quad (2.5)$$

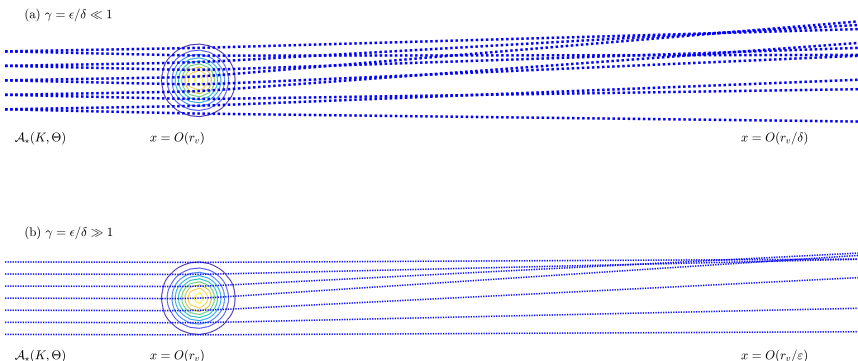


Figure 1: The scattering problem: a localised flow, here shown as an axisymmetric vortex with radius r_v , scatters waves incident from the left ($x \rightarrow -\infty$) with action spectrum $\mathcal{A}_*(K, \Theta)$. Rays bend significantly only in the scattering region in which there is non-zero vorticity i.e. where $x = O(r_v)$. In this illustration r_v is equivalent to ℓ_s . (a) The case $\delta \neq 0$: directional spreading in the incident spectrum \mathcal{A}_* is indicated schematically by two rays emanating from each source point. (b) The case $\delta = 0$ (or much less than ϵ): the incident spectrum \mathcal{A}_* is a plane wave with little or no directional spreading.

128 The incident swell is characterized by a spatially uniform spectrum $\mathcal{F}_*(\mathbf{k})$
 129 with constant significant wave height H_{s*} . The subscript \star denotes quantities
 130 associated with the incident waves. Swell is characterized by a narrow spectrum
 131 in both wavenumber k (equivalently, frequency σ) and direction θ . The dominant
 132 wavenumber of the incident swell is k_* with frequency $\sigma_* = \sqrt{gk_*}$, and the
 133 dominant direction is taken without loss of generality as $\theta = 0$. Thus, as
 134 illustrated in figure 1, the waves arrive from $x = -\infty$ and impinge on an isolated
 135 flow feature, centred at $(x, y) = (0, 0)$. As an example of incident spectrum we
 136 use a separable construction described in appendix A. In the narrow-band limit
 137 corresponding to swell, this spectrum simplifies to the Gaussian

$$138 \quad \mathcal{F}_*(k, \theta) \approx \zeta_{rms*}^2 \underbrace{\frac{e^{-(k-k_*)^2/2\delta_k^2}}{k_* \sqrt{2\pi\delta_k^2}}}_{F_*(k)} \times \underbrace{\frac{e^{-\theta^2/2\delta_\theta^2}}{\sqrt{2\pi\delta_\theta^2}}}_{D_*(\theta)}. \quad (2.6)$$

139 The two parameters δ_k and δ_θ capture the wavenumber and directional spreading
 140 (see Appendix A). The narrow-band limit assumes that $\delta_k/k_* \ll 1$ and $\delta_\theta \ll 1$.

141 3. The scattering problem

142 We consider an incident spectrum such as (2.6). To make its localisation in k and
 143 θ explicit we introduce the $O(1)$ independent variables

$$144 \quad K = \frac{k - k_*}{\delta} \quad \text{and} \quad \Theta = \frac{\theta}{\delta}, \quad (3.1)$$

145 where $\delta \ll 1$ is a small dimensionless parameter. The incident action spectrum
146 has the form

$$147 \quad \mathcal{A}(x, y, k, \theta) = \mathcal{A}_*(K, \Theta) \quad \text{as } x \rightarrow -\infty, \quad (3.2)$$

148 where the function $\mathcal{A}_*(K, \Theta)$ is localised where both K and Θ are $O(1)$. The
149 example spectrum (2.6) is of this form provided that δ_k/k_* and δ_θ are both $O(\delta)$.
150 This assumption of similarly small spectral widths in k and θ enforces the relevant
151 distinguished limit for the scattering problem.

152 We assume that the currents are weak (e.g. Peregrine 1976; Villas Bôas &
153 Young 2020). This means that the typical speed U of the currents is much less
154 than the intrinsic group velocity of the incident swell c_* :

$$155 \quad \varepsilon \stackrel{\text{def}}{=} U/c_*, \quad (3.3)$$

$$156 \quad \ll 1. \quad (3.4)$$

157 Accordingly we rewrite the frequency (2.2) as

$$158 \quad \omega(\mathbf{x}, \mathbf{k}) = \sigma(k) + \varepsilon \mathbf{k} \cdot \mathbf{U}(\mathbf{x}). \quad (3.5)$$

159 We indulge in a slight abuse of notation here: we develop the approximation in
160 dimensional variables, hence the dimensionless parameters ε and δ in expressions
161 such as (3.1) and (3.5) should be interpreted as bookkeeping parameters to be
162 set to one at the end. We examine the distinguished limit

$$163 \quad \delta, \varepsilon \rightarrow 0 \quad \text{with} \quad \gamma \stackrel{\text{def}}{=} \varepsilon/\delta = O(1) \quad (3.6)$$

164 and use matched asymptotics to solve the action conservation equation (2.1). We
165 emphasise that $\gamma = O(1)$ is a formal assumption that enables us to capture the
166 broadest range of relative size of ε and δ , including $\varepsilon \ll \delta$ and $\delta \ll 1$ (see §5).

167 3.1. The scattering region: $x = O(\ell_s)$

168 The spatially compact flow has a typical horizontal length scale which we denote
169 by ℓ_s . We refer to the region where $x = O(\ell_s)$ as the ‘scattering region’. The
170 solution in this region has the form

$$171 \quad \mathcal{A}(K, \Theta, x, y) \quad (3.7)$$

172 and must limit to $\mathcal{A}_*(K, \Theta)$ in (3.2) as $x \rightarrow -\infty$.

173 With \mathcal{A} in (3.7) the transport term in (2.1) is approximated as

$$174 \quad \begin{aligned} \nabla_{\mathbf{k}} \omega \cdot \nabla_{\mathbf{x}} \mathcal{A} &= c_* (\cos(\delta\Theta) \mathcal{A}_x + \sin(\delta\Theta) \mathcal{A}_y) + \varepsilon \mathbf{U} \cdot \nabla_{\mathbf{x}} \mathcal{A} \\ 175 \quad &= c_* \mathcal{A}_x + O(\delta, \varepsilon). \end{aligned} \quad (3.8)$$

176 In particular, transport by the current, $\varepsilon \mathbf{U} \cdot \nabla_{\mathbf{x}} \mathcal{A}$ is negligible compared with
177 transport by the intrinsic group velocity c_* . With the approximations

$$178 \quad \nabla_{\mathbf{k}} \mathcal{A} = \delta^{-1} (\partial_K \mathcal{A} \hat{\mathbf{x}} + k_*^{-1} \partial_\Theta \mathcal{A} \hat{\mathbf{y}}) + O(1), \quad (3.9)$$

$$179 \quad \nabla_{\mathbf{x}} \omega = \varepsilon k_* (U_x \hat{\mathbf{x}} + U_y \hat{\mathbf{y}}) + O(\varepsilon \delta), \quad (3.10)$$

180 the refraction term in (2.1) simplifies to

$$181 \quad \nabla_{\mathbf{x}} \omega \cdot \nabla_{\mathbf{k}} \mathcal{A} = \gamma (k_* U_x \partial_K \mathcal{A} + U_y \partial_\Theta \mathcal{A}) + O(\varepsilon). \quad (3.11)$$

182 Thus in the scattering region the leading-order approximation to (2.1) is

$$183 \quad c_* \partial_x \mathcal{A} - \gamma (k_* U_x \partial_K \mathcal{A} + U_y \partial_\Theta \mathcal{A}) = 0, \quad (3.12)$$

184 One might solve (3.12) using its characteristics – the ray equations – or by
 185 inspection. By either method the solution to (3.12) that matches the incident
 186 action spectrum (3.2) as $x \rightarrow -\infty$ is found to be

$$187 \quad \mathcal{A}(x, y, K, \Theta) = \mathcal{A}_* \left(K + \frac{\gamma k_*}{c_*} U(x, y), \Theta + \frac{\gamma}{c_*} \int_{-\infty}^x U_y(x', y) dx' \right). \quad (3.13)$$

188 It is insightful to introduce the vorticity $Z \stackrel{\text{def}}{=} V_x - U_y$ and write (3.13) as

$$189 \quad \mathcal{A}(x, y, K, \Theta) = \mathcal{A}_* \left(K + \frac{\gamma k_*}{c_*} U(x, y), \Theta + \frac{\gamma}{c_*} V(x, y) - \frac{\gamma}{c_*} \int_{-\infty}^x Z(x', y) dx' \right). \quad (3.14)$$

190 For reference, we rewrite this expression in terms of the original independent
 191 variables, setting the bookkeeping parameters ε , δ , and hence γ to 1 to obtain

$$192 \quad \mathcal{A}(x, y, k, \theta) = \mathcal{A}_* \left(k + \frac{k_*}{c_*} U(x, y), \theta + \frac{1}{c_*} V(x, y) - \frac{1}{c_*} \int_{-\infty}^x Z(x', y) dx' \right). \quad (3.15)$$

193 3.2. The intermediate region: $O(\ell_s) \ll x \ll O(\ell_s/\delta)$

194 The outer limit of the inner solution (3.14) follows from taking $x \rightarrow \infty$:

$$195 \quad \mathcal{A}(x, y, K, \Theta) \rightarrow \mathcal{A}_* (K, \Theta - \gamma \Delta(y)), \quad (3.16)$$

196 where we have introduced the dimensionless ‘deflection’

$$197 \quad \Delta(y) \stackrel{\text{def}}{=} \frac{1}{c_*} \int_{-\infty}^{\infty} Z(x', y) dx'. \quad (3.17)$$

198 According to (3.16) the effect of the flow on the dependence of \mathcal{A} on K is
 199 reversible: after passage through the scattering region this dependence reverts
 200 to the incident form. In contrast, there is a net change in Θ , quantified by the
 201 deflection $\Delta(y)$. This can be related to classical scattering of particles by viewing
 202 y as the impact parameter of a wavepacket. The scattering cross section, defined
 203 as $dy/d\theta_\infty$ where θ_∞ is the angle of propagation of the wavepacket as $x \rightarrow \infty$, is
 204 then $-1/(\varepsilon \Delta'(y))$.

205 To physically interpret (3.16) and $\Delta(y)$, recall that if ε is small then

$$206 \quad \text{ray curvature} \approx \frac{\text{vorticity}}{\text{group velocity}}, \quad (3.18)$$

$$207 \quad \approx \frac{Z(x, y)}{c_*}. \quad (3.19)$$

208 The approximation in (3.18) requires only $\varepsilon \ll 1$ (e.g. Kenyon 1971; Landau &
 209 Lifshitz 2013; Dysthe 2001; Gallet & Young 2014). Passing from (3.18) to (3.19)
 210 requires the further approximation that k is close to k_* so that the group velocity
 211 in the denominator of (3.18) can be approximated by the constant c_* . On the left
 212 of (3.18) ray curvature is $d\theta/d\ell$, where ℓ is arc-length along a ray. But within
 213 the compact scattering region we approximate ℓ with x . Thus the deflection $\Delta(y)$
 214 in (3.17) is the integrated ray curvature, accumulated as rays pass through the
 215 scattering region in which $x = O(\ell_s)$ and vorticity $Z(x, y)$ is non-zero.

216 From (3.17) and (3.18) we conclude that the scattering region is best charac-
 217 terized as the region with $O(1)$ vorticity, e.g. the vortex core in figure 1 (hence
 218 $\ell_s = r_v$ with r_v a typical vortex radius). The region with palpably non-zero

219 velocity is much larger. In figure 1 the rays are straight where $x = O(r_v/\varepsilon)$,
 220 despite the slow ($\propto r^{-1}$) decay of the azimuthal vortex velocity.

221 3.3. The far field: $x = O(\ell_s/\delta)$

222 Far from the scattering region, where $x \gg \ell_s$, we introduce the slow coordinate
 223 $X \stackrel{\text{def}}{=} \delta x$. In the far-field the currents and hence the refraction term $\nabla_{\mathbf{x}}\omega \cdot \nabla_{\mathbf{k}}\mathcal{A}$
 224 in (2.1) are negligible. The steady action conservation equation collapses to

$$225 \quad \nabla_{\mathbf{k}}\sigma \cdot \nabla_{\mathbf{x}}\mathcal{A} = c_* (\delta \cos(\delta\theta)\mathcal{A}_X + \sin(\delta\theta)\mathcal{A}_y) = 0, \quad (3.20)$$

226 i.e. propagation along straight rays. Retaining only the leading-order term gives

$$227 \quad \partial_X \mathcal{A} + \Theta \partial_y \mathcal{A} = 0, \quad (3.21)$$

228 By inspection the solution of (3.21) that matches the intermediate solution (3.16)
 229 is

$$230 \quad \mathcal{A}(X, y, K, \Theta) = \mathcal{A}_*(K, \Theta - \gamma \Delta(y - X\Theta)). \quad (3.22)$$

231 This formula, which converts the incident spectrum into the far-field spectrum,
 232 is a key result of the paper. In terms of the original independent variables and
 233 with the bookkeeping parameters set to 1 it takes the convenient form

$$234 \quad \mathcal{A}(x, y, k, \theta) = \mathcal{A}_*(k, \theta - \Delta(y - x\theta)). \quad (3.23)$$

235 3.4. Significant wave height

236 Significant wave height H_s is the most commonly reported statistic of wave
 237 amplitudes, being routinely observed by satellite altimeters and wave buoys. We
 238 obtain an approximation for H_s by performing the k and θ integrals in (2.5) using
 239 the approximations (3.15) and (3.23) for $\mathcal{A}(\mathbf{x}, \mathbf{k})$.

240 The scattering region is simple. We can approximate σ and $d\mathbf{k}$ in (2.5) by
 241 $\sigma_* = \sigma(k_*)$ and $k_* dk d\theta$ to find

$$242 \quad H_s(\mathbf{x}, t) \sim \left(\frac{16\sigma_* k_*}{g} \iint \mathcal{A}(\mathbf{k}, \mathbf{x}, t) dk d\theta \right)^{1/2} \quad (3.24)$$

$$243 \quad \sim H_{s*} \quad (3.25)$$

244 The second equality holds because, according to (3.15), $\mathcal{A}(\mathbf{x}, \mathbf{k})$ is obtained from
 245 $\mathcal{A}_*(\mathbf{x}, \mathbf{k})$ by an \mathbf{x} -dependent shift of the k and θ that does not affect the integral.
 246 Thus H_s in the scattering region is unchanged from the incident value H_{s*} . This
 247 conclusion also follows directly from steady-state wave action conservation under
 248 the assumptions $\varepsilon, \delta \ll 1$: multiplying (3.12) by $\sigma_* k_*$ and integrating over k and
 249 θ we find

$$250 \quad c_* \partial_x \underbrace{\left(\sigma_* k_* \iint \mathcal{A}(\mathbf{x}, \mathbf{k}) dk d\theta \right)}_{\approx g H_s^2(\mathbf{x})/16} = 0. \quad (3.26)$$

251 Hence $H_s(\mathbf{x}) = H_{s*}$ throughout the scattering region.

252 In the far field, H_s is obtained by substituting (3.23) into (2.5). The result is

$$253 \quad H_s(\mathbf{x}) = 4 \sqrt{\frac{k_* \sigma_*}{g} \int d\theta \int dk \mathcal{A}_*(k, \theta - \Delta(y - x\theta))}. \quad (3.27)$$

254 The k -integral can be evaluated in terms of the incident directional spectrum
 255 which, in the general case of a non-separable spectrum, is defined as

$$256 \quad D_*(\theta) \stackrel{\text{def}}{=} \frac{1}{\zeta_{rms}^2} \int \mathcal{F}_*(\mathbf{k}) k \, d\mathbf{k}. \quad (3.28)$$

257 We summarize the results above with:

$$258 \quad H_s(\mathbf{x}) = H_{s*} \begin{cases} 1 & \text{in the scattering region,} \\ \sqrt{\int D_*(\theta - \Delta(y - x\theta)) \, d\theta} & \text{in the far field.} \end{cases} \quad (3.29)$$

259 4. Applications to simple flows

260 4.1. Gaussian vortex

261 As an application, we consider scattering by an axisymmetric Gaussian vortex
 262 with circulation κ , vorticity

$$263 \quad Z(x, y) = \frac{\kappa e^{-r^2/2r_v^2}}{2\pi r_v^2}, \quad (4.1)$$

264 and velocity

$$265 \quad (U(x, y), V(x, y)) = \frac{\kappa}{2\pi} \frac{1 - e^{-r^2/2r_v^2}}{r^2} (-y, x), \quad (4.2)$$

266 where $r^2 = x^2 + y^2$. The vortex radius r_v can be taken as the scattering length
 267 scale ℓ_s . The maximum azimuthal velocity is $U_m = 0.072 \kappa/r_v$ at radius $1.585 r_v$.
 268 The deflection (3.17) resulting from this Gaussian vortex is

$$269 \quad \Delta(y) = \frac{\kappa e^{-y^2/2r_v^2}}{\sqrt{2\pi} r_v c_*}. \quad (4.3)$$

270 The asymptotic solution in the scattering region is obtained from (3.15) as

$$271 \quad \mathcal{A}(x, y, k, \theta) = \mathcal{A}_* \left(k + k_* c_*^{-1} U(x, y), \right. \\ 272 \quad \left. \theta + c_*^{-1} V(x, y) - \frac{1}{2} \left(\text{erf}(x/\sqrt{2}r_v) + 1 \right) \Delta(y) \right), \quad (4.4)$$

273 where erf is the error function. Eq. (4.4) can be combined with the far-field
 274 approximation (3.23) into a single, uniformly valid approximation,

$$275 \quad \mathcal{A}(x, y, k, \theta) = \mathcal{A}_* \left(k + k_* c_*^{-1} U(x, y), \right. \\ 276 \quad \left. \theta + c_*^{-1} V(x, y) - \frac{1}{2} \left(\text{erf}(x/\sqrt{2}r_v) + 1 \right) \Delta(y - x\theta) \right). \quad (4.5)$$

277 The significant wave height is approximated by (3.29) which can be written as
 278 the uniform expression

$$279 \quad H_s(x, y) = H_{s*} \sqrt{\int D_*(\theta - \Delta(y - x^+\theta)) \, d\theta}, \quad (4.6)$$

280 where x^+ is equal to x for $x > 0$ and to 0 for $x < 0$ and (4.3) is used for Δ .

281 We now compare the matched asymptotic (MA hereafter) predictions (4.5)–
 282 (4.6) with numerical solutions of the wave action equation (2.1) obtained with

s	U_m (m s ⁻¹)	$\delta = \sqrt{2/s}$	$\varepsilon = U_m/c_\star$	$\gamma = \varepsilon/\delta$
10	0.4	0.447 (25.6°)	0.05	0.112
40	0.4	0.224 (12.8°)	0.05	0.224
10	0.8	0.447 (25.6°)	0.1	0.224
40	0.8	0.224 (12.8°)	0.1	0.447

Table 1: Parameters corresponding to each configuration in section 4.1, arranged in the order of the rows in figure 3. In all cases the group speed is $c_\star = 8$ m s⁻¹, corresponding to a 166 m wavelength and 10.3 s period. U_m is the maximum vortex velocity and the vortex radius is $r_v = 50$ km.

283 the Wave Height, Water Depth, and Current Hindcasting third generation wave
 284 model (WAVEWATCH III, hereafter WW3). The incident spectrum used for
 285 WW3 is described in Appendix A. The directional function for this spectrum is
 286 the Longuet-Higgins *et al.* (1963) model

$$287 \quad D_\star(\theta) \propto \cos^{2s} \frac{\theta}{2}. \quad (4.7)$$

288 The parameter $s > 0$ controls the directional spreading: for $s \gg 1$, (4.7) reduces to
 289 the Gaussian in (2.6) with directional spreading $\delta_\theta = \sqrt{2/s}$. The configuration of
 290 WW3 and spectrum parameters are detailed in Appendix B. The most important
 291 parameter is the peak frequency of the incident spectrum, taken fixed for all
 292 simulations as $\sigma_\star = 0.61$ rad s⁻¹. This corresponds to a period of 10.3 s,
 293 wavelength of 166 m and group speed $c_\star = 8$ m s⁻¹. Because the problem is linear
 294 in the action density, the values of $\zeta_{rms\star}$ or equivalently $H_{s\star}$ are less important.
 295 For definiteness we set $H_{s\star} = 1$ m.

296 Figure 2 compares the wavenumber-integrated wave action $\int \mathcal{A}(x, y, k, \theta) dk$
 297 obtained from (4.5) and WW3 for a Gaussian vortex with maximum velocity
 298 $U_m = 0.8$ m s⁻¹ and directional spreading parameter $s = 40$. Figure 2 shows a
 299 good agreement, especially in the far-field region ($x \geq 3r_v$). The most noticeable
 300 difference between MA and WW3 is in panels c and d, which show a section
 301 through the middle of the vortex. The MA action spectrum in panel d is obtained
 302 via a y -dependent shift in $\mathcal{A}_\star(k, \theta)$; there is no change in the intensity of \mathcal{A}
 303 associated with this shift. In panel c, on the other hand, the intensity of the WW3
 304 action spectrum varies with y/r_v . We attribute this difference to asymptotically
 305 small effects such as the contribution $\mathbf{U} \cdot \nabla_{\mathbf{x}} \mathcal{A}$ to wave-action transport.

306 In the remainder of this section, we assess the dependence of significant wave
 307 height H_s on the directional spreading parameter s and flow strength U_m . We
 308 consider the four different combinations of s and U_m given in Table 1. The
 309 corresponding values of the dimensionless parameters, taken as

$$310 \quad \delta = \delta_\theta = \sqrt{2/s} \quad \text{and} \quad \varepsilon = U_m/c_\star, \quad (4.8)$$

311 are also in the table.

312 Observations of the directional spreading for swell typically range between 10°–
 313 20° (Ewans 2002), which correspond to a range of s between 16 and 66. In our
 314 experiments, setting $s = 10$ and $s = 40$ leads to a directional spreading of 24°
 315 and 12° respectively, which correspond to very broad and very narrow swells.

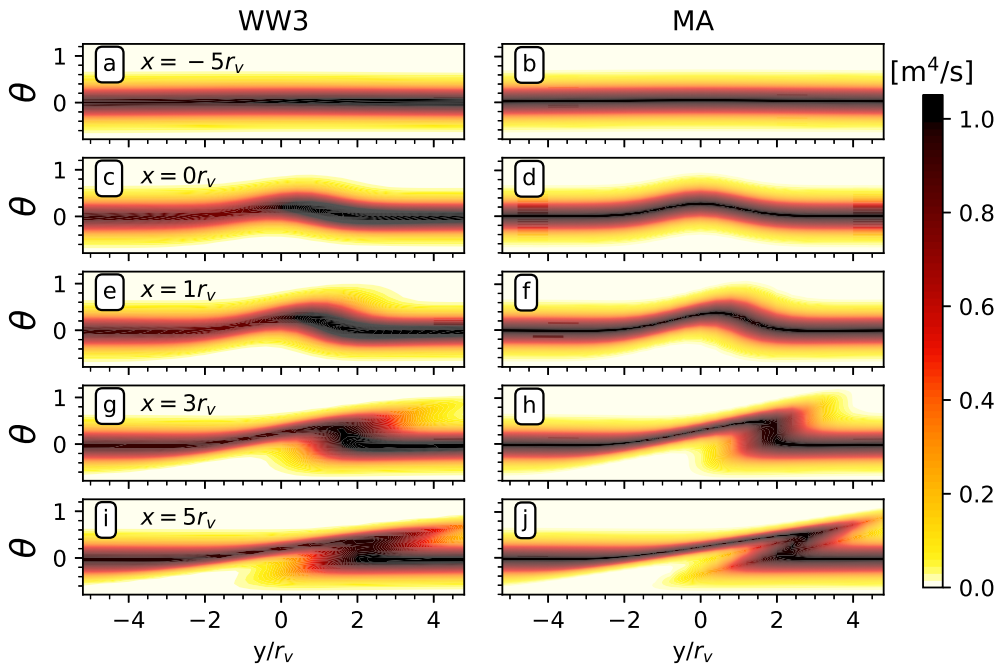


Figure 2: Wavenumber-integrated action density $\int \mathcal{A}(x, y, k, \theta) dk$ as a function of y and θ at $x = -5r_v, 0, r_v, 3r_v$ and $5r_v$ from WW3 (left) and MA (Eq. (4.5), right) for swell impinging on a Gaussian vortex with $U_m = 0.8 \text{ m s}^{-1}$. The directional spreading of the incident spectrum is $s = 40$.

316 Figures 3 and 4 show the significant wave height anomaly

$$317 \quad h_s(\mathbf{x}) \stackrel{\text{def}}{=} H_s(\mathbf{x}) - H_{s\star} \quad (4.9)$$

318 for each combination of s and U_m . Because of our choice of $H_{s\star} = 1\text{m}$, h_s in cm
 319 can be interpreted as the fractional change in significant wave height expressed
 320 as a percentage. A control run of WW3 in the absence of currents shows that h_s
 321 is not exactly zero but decreases slowly with x . This is caused by the finite y -
 322 extent of the computational domain which leads to a wave forcing with compact
 323 support. To mitigate this numerical artefact, we compute the WW3 significant
 324 wave height anomaly as $h_s(\mathbf{x}) = H_s(\mathbf{x}) - H_s^{\text{ctrl}}(\mathbf{x})$, where $H_s^{\text{ctrl}}(\mathbf{x})$ is the significant
 325 wave height of the current-free control run. See Appendix B for details.

326 Figures 3 and 4 show that h_s has a wedge-like pattern in the wake of the
 327 vortex resulting from wave focussing and defocussing, with $h_s > 0$ mainly for
 328 $y > 0$ and $h_s < 0$ for $y < 0$. The pattern is not anti-symmetric about $y = 0$,
 329 and positive anomalies are larger than negative anomalies. These characteristics,
 330 which indicate a nonlinear response, are increasingly marked as s and U_m increase.
 331 Specifically, the parameter

$$332 \quad \gamma = \frac{\varepsilon}{\delta} = \frac{U_m}{c_\star} \sqrt{\frac{s}{2}} \quad (4.10)$$

333 controls the degree of nonlinearity and hence of asymmetry. We discuss the two
 334 limiting regimes $\gamma \ll 1$ and $\gamma \gg 1$ in §5.

335 There is good overall agreement between WW3 and MA, even though, in the

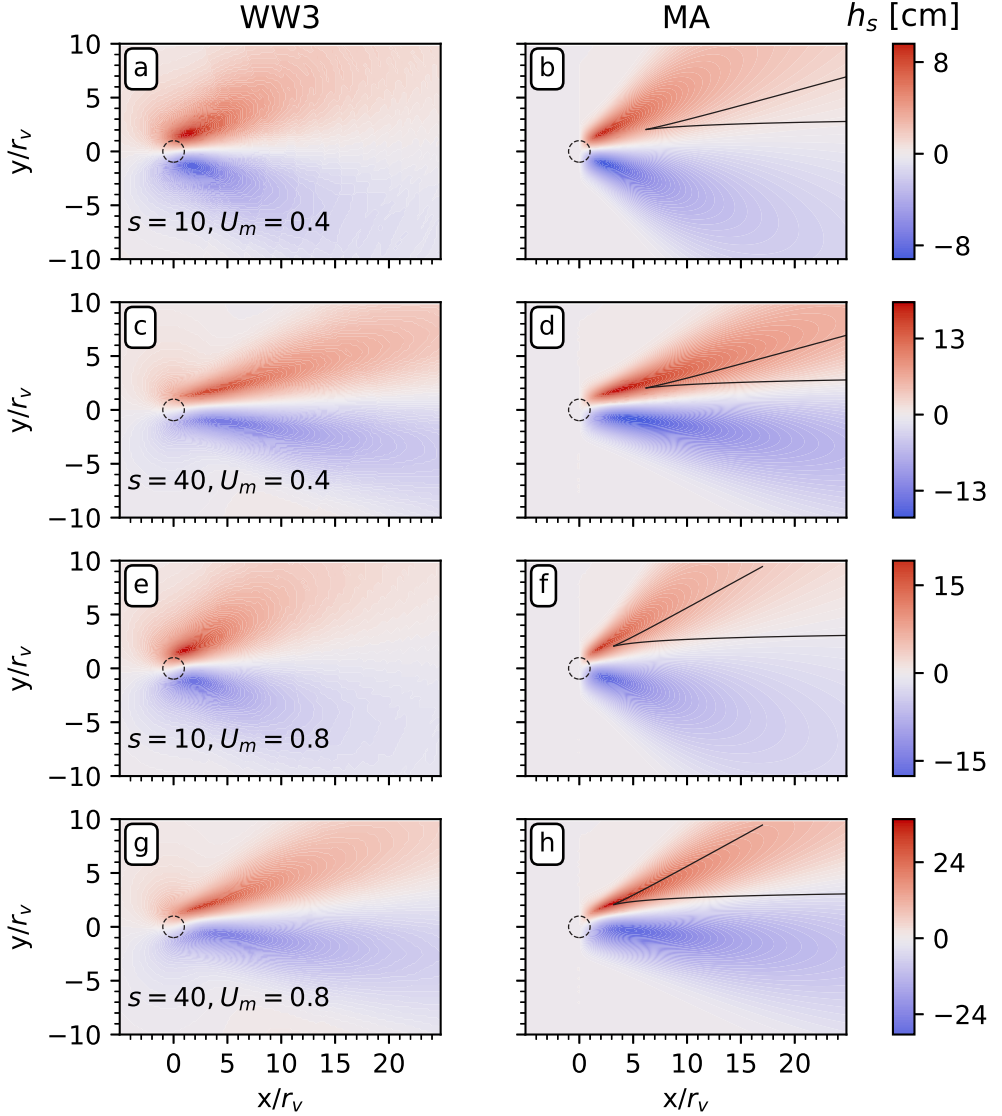


Figure 3: Significant wave height anomaly $h_s(x, y)$ from WW3 (left column) and

MA (right column) for swell impinging on a Gaussian vortex. Each row corresponds to the indicated values of the directional spreading parameter s of the incident wave spectrum and of the maximum velocity U_m (in m s^{-1}). The corresponding non-dimensional parameters are given in Table 1. The dashed circles has radius r_v around vortex center. The solid lines on the right panels indicate the caustics computed from (D 6). The colourbars differ between rows but are the same within each row. White corresponds to $h_s = 0$ in all panels. The customizable notebook that generates panel (h) by default can be accessed at <https://shorturl.at/fswA3>.

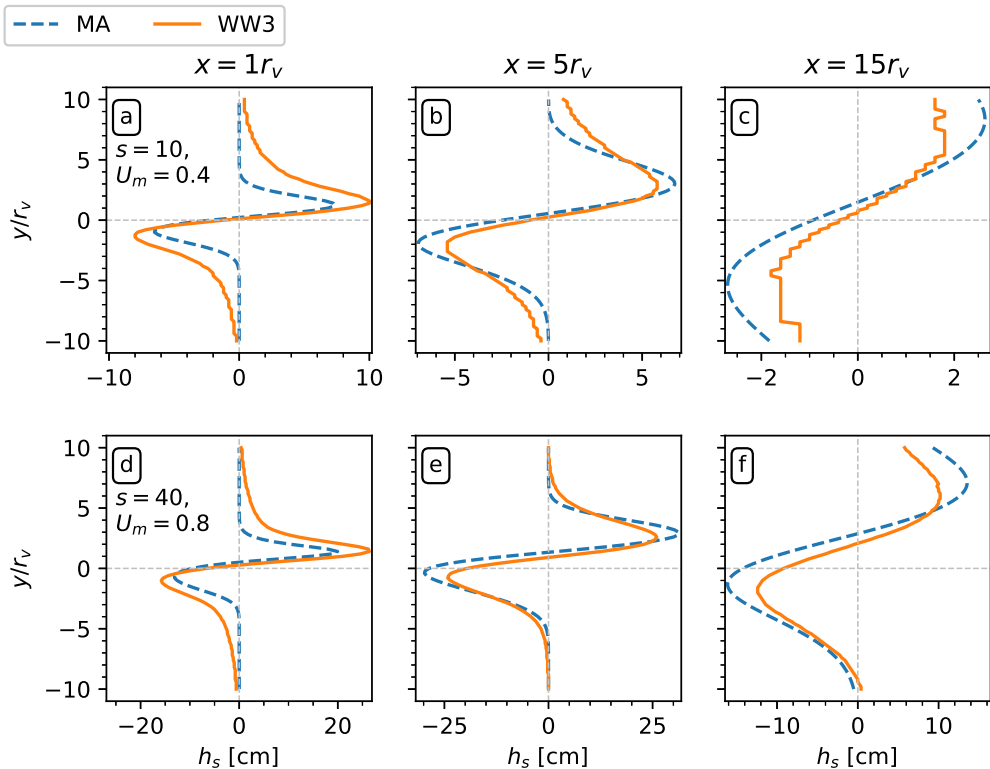


Figure 4: Significant wave height anomaly h_s as a function of y for $x = r_v, 5r_v, 15r_v$ (left, centre and right) from WW3 (solid lines) and MA (Eq. (4.5), dashed lines) in the set up of figure 3. Results are shown for two sets of parameters s and U_m as indicated in the leftmost panels. The range of h_s differs between panels.

336 case $s = 10$, the parameter $\delta = 0.447$ is only marginally small. The pattern is
 337 more diffuse for WW3 than for MA, with a less sharply defined wedge and a non-
 338 zero h_s over a larger proportion of the domain. We attribute the differences to the
 339 finiteness of δ (they are more marked for $s = 10$, $\delta = 0.447$ than for $s = 40$, $\delta =$
 340 0.224), and to the limited spectral resolution of WW3 (simulations with degraded
 341 angular resolution lead to an even more diffuse h_s). The most conspicuous
 342 differences between WW3 and MA appear in the scattering region, where the
 343 non-zero h_s obtained with WW3 appears to contradict the MA prediction that
 344 $h_s = 0$. The non-zero h_s results from $O(\varepsilon, \delta)$ terms neglected by MA. Relaxing
 345 some of the approximations leading to (3.24) gives a heuristic correction to MA
 346 that captures the bulk of the difference with WW3 in the scattering region. We
 347 explain this in Appendix C.

348 As further demonstration of the MA approach, we provide a Jupyter notebook
 349 accessible at <https://shorturl.at/fswA3>, where users can customize the form
 350 of the current and the incoming wave spectrum to experiment with the resulting
 351 $\int \mathcal{A}(x, y, k, \theta) dk$ and h_s .

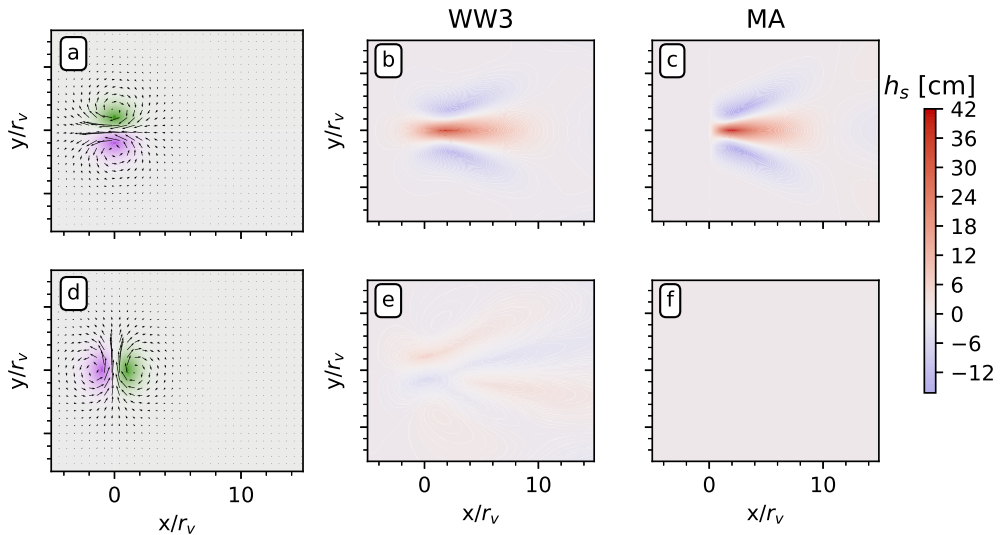


Figure 5: Swell impinging on vortex dipoles with axes perpendicular (top) and parallel (bottom) to the dominant direction of wave propagation (x -axis). The vorticity (colour) and velocity (vectors) are shown (left) together with the significant wave height anomaly h_s from WW3 (middle) and MA (right). The directional spreading parameter $s = 40$ and the maximum flow velocity is 0.8 m s^{-1} .

352

4.2. Vortex dipole

353 A striking feature of the far-field spectrum and hence of H_s is that, according to
 354 MA, they depend on the flow only through the deflection $\Delta(y)$ in (3.17), propor-
 355 tional to the integral of the vorticity along the direction of dominant wave propa-
 356 gation (the x -direction in our set up). This implies that if the integrated vorticity
 357 vanishes because of cancellations between positive and negative contributions, the
 358 differences between far-field and incident fields are asymptotically small. This can
 359 be interpreted as a form of ‘vortex cloaking’, whereby an observer positioned well
 360 downstream of a flow feature is unable to detect its presence through changes in
 361 wave statistics. We demonstrate this phenomenon by examining the scattering of
 362 swell by vortex dipoles.

363 We consider two cases, corresponding to dipoles whose axes (the vector joining
 364 the centres of positive and negative vorticity) are, respectively, perpendicular and
 365 parallel to the direction of wave propagation. The corresponding vorticity fields
 366 are chosen, up to a constant multiple, as the derivative of the Gaussian profile
 367 (4.1) with respect to y or x . Figure 5 shows the significant wave height anomaly
 368 obtained for the incident spectrum of §4.1 with $s = 40$ and dipoles with maximum
 369 velocity $U_m = 0.8 \text{ m s}^{-1}$.

370 When the dipole axis is in the y -direction (top row) the deflection $\Delta(y)$ does not
 371 vanish identically. As a result, H_s is affected by the flow, strongly for our choice
 372 of parameters. This applies to both the MA and WW3 predictions which match
 373 closely in the far field. When the dipole axis is in the x -direction (bottom row),
 374 $\Delta(y) = 0$. The MA prediction is then that $H_s = H_{s*}$, i.e. $h_s = 0$, everywhere.
 375 The WW3 simulation is consistent with this, with only a weak signal in h_s .

376 In general, for a dipole with axis making an angle α with the direction of wave

377 propagation, the deflection $\Delta(y)$ is proportional to $\sin \alpha$ and the cloaking effect
378 is partial unless $\alpha = 0$.

379 5. Limiting cases

380 In this section, we return to the far-field asymptotics (3.22) for \mathcal{A} in terms of the
381 scaled dependent variables in order to examine two limiting regimes characterized
382 by extreme values of $\gamma = \varepsilon/\delta$. The regime $\gamma \ll 1$ corresponds to a weak flow
383 and/or relatively broad spectrum, leading to a linear dependence of h_s on the
384 currents. The opposite regime $\gamma \gg 1$ corresponds to strong flow and/or highly
385 directional spectrum. The wave response is then highly nonlinear in the currents
386 and, as we show below, controlled by the caustics that exist for pure-plane incident
387 waves ($\gamma = \infty$). Heller *et al.* (2008)'s 'freak index', given by $\varepsilon^{2/3}/\delta$, is the analogue
388 of γ for spatially extended, random currents.

389 5.1. Linear regime: $\gamma \ll 1$

390 For $\gamma \ll 1$, we can expand (3.22) in Taylor series to obtain

$$391 \quad \mathcal{A}(X, y, K, \Theta) = \mathcal{A}_*(K, \Theta) - \gamma \Delta(y - X\Theta) \partial_\Theta \mathcal{A}_*(K, \Theta) + O(\gamma^2). \quad (5.1)$$

392 This indicates that the flow induces the small correction $-\gamma \Delta(y - X\Theta) \partial_\Theta \mathcal{A}_*(K, \Theta)$
393 to the action of the incident wave. We deduce an approximation for H_s by
394 integrating (5.1) with respect to K and Θ to obtain H_s^2 followed by a Taylor
395 expansion of a square root. Alternatively, we can carry out a Taylor expansion
396 of the far-field approximation (3.29) of H_s , treating $\Delta(y)$ as small. The result is
397 best expressed in terms of the anomaly h_s , found to be

$$398 \quad h_s(x, y) = -\frac{H_{s*}}{2} \int D'_s(\theta) \Delta(y - x\theta) d\theta \quad (5.2)$$

399 after reverting to the unscaled variables and setting $\gamma = 1$. This simple expression
400 is readily evaluated once the flow, hence $\Delta(y)$, and directional spectrum $D_*(\theta)$
401 are specified. For the Gaussian vortex of §4.1 and the directional spectrum in
402 (2.6), the integration can be carried out explicitly, yielding

$$403 \quad h_s(x, y) = \frac{H_{s*} \kappa}{c_* \sqrt{\pi}} \frac{x^+ y e^{-y^2/(2r_v^2 + 4x^2/s)}}{(2r_v^2 + 4x^2/s)^{3/2}}. \quad (5.3)$$

404 This formula makes it plain that h_s depends on space through $(x/\sqrt{s}, y)$,
405 is antisymmetric about the x axis, and is maximised along the curves
406 $y = \pm \sqrt{r_v^2 + 2x^2/s}$. Decay as $|\mathbf{x}| \rightarrow \infty$ is slowest along these curves and
407 proportional to x^{-1} .

408 We illustrate (5.3) and assess its range of validity by comparing it with MA
409 for two sets of parameters in figure 6. The match is very good for $s = 10$ and
410 $U_m = 0.4 \text{ m s}^{-1}$ (top row), corresponding to $\gamma = 0.112$. It is less good for $s = 40$
411 and $U_m = 0.8 \text{ m s}^{-1}$, unsurprisingly since $\gamma = 0.447$ is not particularly small and
412 the MA prediction is obviously far from linear, with a pronounced asymmetry.
413 The curves $y = \pm \sqrt{r_v^2 + 2x^2/s}$ shown in the figure are useful indicators of the
414 structure of h_s for small enough γ .

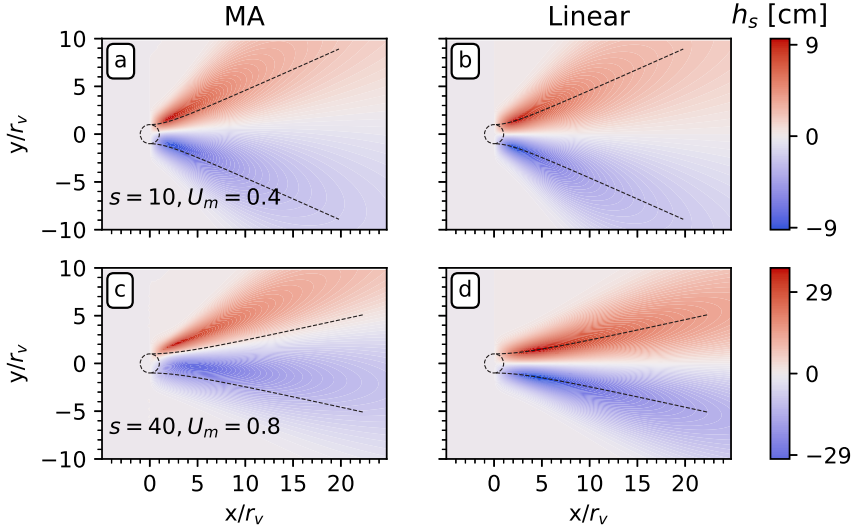


Figure 6: Significant wave height anomaly $h_s(x, y)$ for swell impinging on a Gaussian vortex: comparison between the predictions of MA (left) and its $\gamma \rightarrow 0$ limit ((5.3), right column). The set up is as in figure 3 with parameters s and U_m (in m s^{-1}) as indicated. Dashed lines indicate the curves $y = \pm\sqrt{r_v^2 + 2x^2/s}$ where h_s reach maximum amplitudes according to (5.3).

415

5.2. Caustic regime: $\gamma \gg 1$

416

417

418

The limit $\gamma \rightarrow \infty$ corresponds to an incident wave field that is almost a plane wave. It is natural to rescale variables according to $\Theta \mapsto \gamma\Theta$ and $X \mapsto \gamma^{-1}X$ so that (3.22) becomes

419

$$\mathcal{A}(X, y, K, \Theta) = \mathcal{A}_*(K, \gamma\mathcal{S}(X, y, \Theta)), \quad (5.4)$$

420

where

421

$$\mathcal{S}(X, y, \Theta) \stackrel{\text{def}}{=} \Theta - \Delta(y - X\Theta). \quad (5.5)$$

422

423

424

425

426

In (X, y, Θ) -space, the K -integrated action is concentrated in a thin $O(\gamma^{-1})$ layer around the surface $\mathcal{S}(X, y, \Theta) = 0$. Quantities such as H_s obtained by further integrating the action with respect to Θ can be obtained by approximating the dependence of right-hand side of (5.4) on \mathcal{S} by $\delta(\mathcal{S})$. This fails, however, when (X, y, Θ) satisfy both

427

$$\mathcal{S}(X, y, \Theta) = 0, \quad \text{and} \quad \partial_\Theta \mathcal{S}(X, y, \Theta) = 1 + X\Delta'(y - X\Theta) = 0. \quad (5.6)$$

428

429

430

431

432

433

434

The corresponding curves in the (X, y) plane are caustics near which $\int \mathcal{A}(X, y, K, \Theta) dK d\Theta$ is an order $\gamma^{1/2}$ larger than elsewhere; correspondingly, $H_s = O(\gamma^{1/4})$. In figure 7 the two caustics meet at a cusp point from opposite sides of a common tangent. The cusp point is located by the condition $\partial_\Theta^2 \mathcal{S} = 0$ and the integrated action at the cusp point is $O(\gamma^{2/3})$ so that $H_s = O(\gamma^{1/3})$. We have numerically verified these γ -scalings at the caustics and at the cusp point by varying s in the MA solutions.

435

436

437

For the Gaussian vortex (4.1), the system (5.6) can be solved to obtain an explicit equation for the caustics. This equation is derived in Appendix D and given by (D6). It describes two curves $y(x)$ emanating from the cusp point at

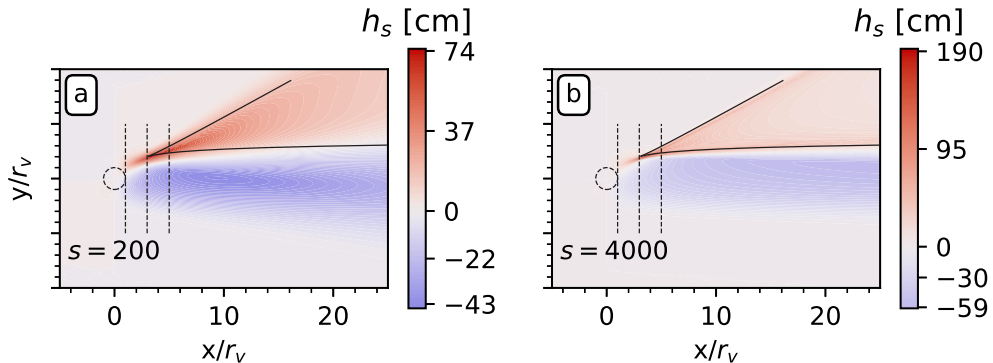


Figure 7: Caustics for swell impinging on a Gaussian vortex: the caustics (D 6) (solid lines) are superimposed to the MA prediction of h_s for $U_m = 0.8 \text{ m s}^{-1}$ and the indicated values of s . The dashed vertical lines correspond to the values of $x = r_v, 3r_v$ and $5r_v$ used in figure 8.

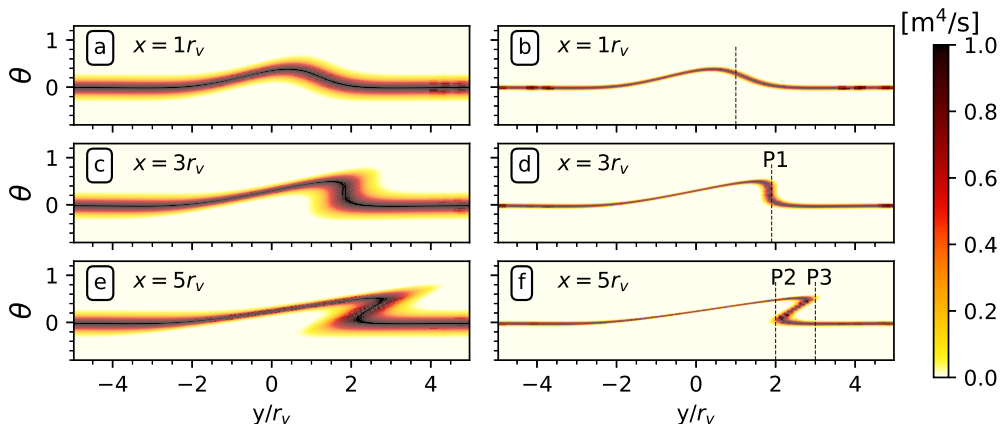


Figure 8: Wavenumber-integrated action density $\int \mathcal{A}(x, y, k, \theta) dk$ as a function of y and θ for $x = r_v, 3r_v$ and $5r_v$ corresponding to the significant wave height shown in figure 7 for $s = 200$ (left column) and $s = 4000$ (right column). P1 in panel d corresponds to the values of (x, y) of the cusp from where the caustics emanate; P2 and P3 are associated to points on each of the two caustics.

438 $x = x_c$ given by (D 5). The caustics (which depend on U_m but not on s) are
 439 indicated on the right panels of figure 3. For the parameters of the figure, the
 440 caustics do not map regions of particularly large h_s . This is unsurprising since γ
 441 is at most 0.447.

442 To assess how large γ or equivalently s need to be for caustics to be the
 443 dominant feature of H_s , we show in figure 7 h_s computed from MA for $U_m = 0.8 \text{ m}$
 444 s^{-1} and $s = 200$ (left panel, $\gamma = 1$) and $s = 4000$ (right panel, $\gamma = 4.47$). It is only
 445 for $s = 4000$ that the caustics are evidently controlling the significant wave height
 446 pattern. We emphasise that $s = 200$ and a fortiori $s = 4000$ are unrealistically
 447 large values: observational estimates for s in the open ocean seldom exceed $s = 80$.
 448 We conclude that caustics are unlikely to play a role in real ocean conditions.

449 With academic rather than practical interest in mind, then, we show in figure 8

450 the integrated action $\int \mathcal{A} dk$ as a function of y for different three different values
 451 of x (identified by dashed vertical lines in figure 7). The figure illustrates how
 452 caustics emerge from a fold singularity in the surface $\mathcal{S}(x, y, \theta) = 0$ along which
 453 action is concentrated in the (x, y, θ) phase space. For $x = r_v$, the surface is a
 454 graph over (x, y) and there are no caustics; for $x = x_c \approx 3r_v$, the surface has a
 455 single point of vertical tangency (P1 in panel (f) of 7) corresponding to the birth
 456 of caustics at a cusp in the (x, y) -plane; for $x = 5r_c$, there are two points of vertical
 457 tangency, P2 and P3 in panel (h), corresponding to the two caustic curves. The
 458 picture is increasingly blurred as s decreases (compare the right panel of figure 8
 459 with the left panels and with figure 2), explaining the diminishing importance of
 460 caustics for H_s .

461 6. Discussion and conclusion

462 The main results in this study are obtained by approximate solution of the
 463 wave action equation in the four-dimensional position–wavenumber space. A
 464 main organizing principle identified by the analysis is that scattering of SGWs
 465 by spatially compact currents results in the deflection function, $\Delta(y)$ in (3.17).
 466 Although Δ varies linearly with the vertical vorticity of the currents, Δ figures in
 467 a nonlinear transformation of the action density. This nonlinear transformation
 468 produces the modulation of the significant wave height H_s behind the scattering
 469 region, e.g. the expression for H_s in (3.29). Quantities that depend on other
 470 moments (e.g., Stokes drift) behave similarly and could be readily inferred from
 471 our explicit forms (3.15) and (3.22) for the wave action density.

472 While we have obtained these results for deep-water SGWs, they apply essentially
 473 unchanged to other two-dimensional waves with isotropic dispersion relation
 474 such as finite-depth SGWs or Poincaré waves. The conclusions we draw about
 475 H_s can also be rephrased in terms of other root-mean-square quantities relevant
 476 to waves other than SGWs. With a little effort, the approach we adopt, based on
 477 the matched asymptotics treatment of the wave action equation, could be further
 478 extended to three-dimensional waves and to anisotropic dispersion relations. Our
 479 results could easily be extended to account for vertically sheared currents using
 480 the modified dispersion relation of Kirby & Chen (1989) (which involves a Doppler
 481 shift term that is nonlinear in \mathbf{k}).

482 In addition to the WKB approximation used to derive the action conservation
 483 equation (2.1) there are two independent approximations involved:

- 484 (a) the current speed is much less than the group velocity of the incident swell;
- 485 (b) swell with small directional spreading is incident on a region of spatially
 486 compact currents e.g. an axisymmetric vortex or a vortex dipole.

487 Provided that (a) and (b) are satisfied the approximate solution of the wave
 488 action equation compares well with numerical solutions provided by WW3.

489 Approximation (a) is usually justified. To challenge (a) one must consider
 490 current speeds such as 2 m s^{-1} e.g. observed as a peak current speed in the
 491 Agulhas system (Quilfen & Chapron 2019). Swell with 100 m wavelength has
 492 group velocity $\sim 6 \text{ m s}^{-1}$ so that the small parameter in (a) is as large as $1/3$. In
 493 less extreme cases approximation (a) will be satisfied.

494 Approximation (b) is less secure: ocean swell is not sufficiently unidirectional
 495 to strongly justify (b) e.g. see the δ -column in table 1. Over long distances,
 496 the continuous scattering by uncorrelated currents leads to a broadening of the
 497 angular spectrum. When approximation (a) applies, this broadening is described

498 by the directional diffusion equation for wave action derived by Villas Bôas &
 499 Young (2020). This diffusion process is one of the mechanisms that makes swell
 500 with very small values of δ unlikely. However, our computations for a Gaussian
 501 vortex indicate that our asymptotic results are reliable for the moderately small
 502 values of δ typical of swell.

503 Because of the relatively large directional spreading of ocean swell the mathe-
 504 matical ideal of a sharp wave caustic is not realized. Instead the caustic singularity
 505 is ‘washed out’ (Heller *et al.* 2008). Behind a vortex we find instead an elongated
 506 streaky pattern in H_s .

507 Our results show that H_s behind an axisymmetric vortex with parameters in
 508 table 1 has spatial variation as large as $\pm 30\%$ of the incident constant value H_{s*} .
 509 Spatial inhomogeneities in H_s of this magnitude are important for wave breaking
 510 and exchange of momentum, heat and gas between the ocean and atmosphere.
 511 For example, airborne observations of the ocean surface by Romero *et al.* (2017)
 512 indicate that $\pm 30\%$ variations in H_s are associated with an order of magnitude
 513 increase in whitecap coverage.

514 The directional diffusion equation of Villas Bôas & Young (2020) uses only
 515 approximation (a). One does not need to assume that the wave field is strongly
 516 unidirectional or that the currents are spatially compact. Moreover the directional
 517 diffusion equation is obtained without detailed consideration of the perturbations
 518 to the action spectrum that accompany wave scattering. But there is useful
 519 information hiding in these unexamined perturbations to the action spectrum. We
 520 are currently engaged in extracting these perturbations, calculating the attendant
 521 spatial variability to H_s , and relating the statistics of these fluctuations in H_s
 522 to those of the surface currents. These future developments promise to explain
 523 numerical experiments that identify relations between the spectral slopes of
 524 surface-current spectra and those of significant wave height (Villas Boas *et al.*
 525 2020).

526 **Acknowledgements.** We thank Victor Shrira for conversations about this work.

527 **Funding.** JV and HW are supported by the UK Natural Environment Research Council
 528 (grant NE/W002876/1). ABVB is supported by NASA award 80NSSC23K0979 through the
 529 International Ocean Vector Winds Science Team. WRY is supported by the National Science
 530 Foundation award 2048583.

531 **Declaration of interests.** The authors report no conflict of interest.

532 **Data availability statement.** The WW3 configuration files applied in this work can be found
 533 at <https://github.com/biavillasboas/SwellVortex>. The customizable Jupyter Notebook file
 534 demonstrating the matched asymptotics approach is available at <https://shorturl.at/fswA3>.

535 **Author ORCID.** H. Wang, <https://orcid.org/0000-0002-5841-5474>. A. B. Villas Bôas,
 536 <https://orcid.org/0000-0001-6767-6556>. W.R Young, <https://orcid.org/0000-0002-1842-3197>. J.
 537 Vanneste, <https://orcid.org/0000-0002-0319-589X>.

538 Appendix A. Incident spectrum

539 We use the separable spectrum

$$540 \mathcal{F}_*(k, \theta) = \zeta_{rms*}^2 F_*(k) D_*(\theta). \quad (\text{A } 1)$$

541 The wavenumber function in (A 1) is

$$542 \quad F_{\star}(k) \stackrel{\text{def}}{=} \frac{2}{\operatorname{erfc}(-\sigma_{\star}/\sqrt{2}\delta_{\sigma})} \frac{e^{-(\sigma-\sigma_{\star})^2/2\delta_{\sigma}^2}}{\sqrt{2\pi}\delta_{\sigma}^2} \frac{1}{k} \frac{d\sigma}{dk}, \quad (\text{A } 2)$$

543 where erfc is the complementary error function. It corresponds to a Gaussian
544 spectrum in frequency truncated at $\sigma = 0$. The angular part of the spectrum in
545 (A 1) is

$$546 \quad D_{\star}(\theta) \stackrel{\text{def}}{=} \frac{\Gamma(s+1)}{2\sqrt{\pi}\Gamma(s+\frac{1}{2})} \cos^{2s} \left(\frac{\theta}{2} \right) \quad (\text{A } 3)$$

547 (Longuet-Higgins *et al.* 1963), which corresponds to incoming waves spread
548 around $\theta = 0$. The four parameters in this model spectrum are the root mean
549 square sea-surface displacement $\zeta_{rms\star}$, the peak radian frequency $\sigma_{\star} = \sqrt{gk_{\star}}$, the
550 spectral width δ_{σ} and the directional spreading parameter s . Normalization is
551 ensured with

$$552 \quad \int_{-\pi}^{\pi} D_{\star}(\theta) d\theta = 1 \quad \text{and} \quad \int_0^{\infty} F_{\star}(k) k dk = 1. \quad (\text{A } 4)$$

553 In the narrow-band limit $\delta_{\sigma}/\sigma_{\star} \ll 1$ and $s \gg 1$, the spectrum is approximated
554 by (2.6) with $\delta_k = 2\delta_{\sigma}\sqrt{k_{\star}/g}$ and $\delta_{\theta} = \sqrt{2/s}$. The parameter δ_{θ} captures
555 the standard deviation in the angular distribution, which is the definition of
556 ‘directional spreading’ (Kuik *et al.* 1988). We note that the expressions for
557 directional spreading are sometimes formally different, but equivalent to our
558 expression for δ_{θ} at large s . For example, another popular way to state the
559 definition for a generic directional distribution is

$$560 \quad \sigma_{\theta} \stackrel{\text{def}}{=} \left[2 \left(1 - (a^2 + b^2)^{1/2} \right) \right]^{1/2}, \quad (\text{A } 5)$$

561 where

$$562 \quad a = \int \cos \theta D_{\star}(\theta) d\theta \quad \text{and} \quad b = \int \sin \theta D_{\star}(\theta) d\theta \quad (\text{A } 6)$$

563 (Villas Boás *et al.* 2020). Using the expression of D_{\star} in (2.6), we can compute
564 the integrals in (A 6) analytically, getting $a = e^{-1/s}$ and $b = 0$. Therefore,

$$565 \quad \sigma_{\theta}^2 = 2(1 - e^{-1/s}) \rightarrow 2/s \quad \text{as} \quad s \rightarrow \infty. \quad (\text{A } 7)$$

566 Thus the definition of σ_{θ} in (A 5) indeed agrees with the parameter δ_{θ} at large s .

567 Appendix B. Set up of WAVEWATCH III

568 We compare our results with numerical simulations from an idealized setup of
569 WW3 which integrates the action balance equation (2.1). Here, we focus on freely
570 propagating swell-type waves, so the effects of wind forcing, nonlinear interactions
571 and wave breaking are ignored (e.g., Villas Boás *et al.* 2020). We use WW3 version
572 v6.07.1 (<https://github.com/NOAA-EMC/WW3/releases/tag/6.07.1>) to solve
573 (2.1) on a 1000 km \times 1000 km Cartesian domain with 5 km grid spacing. To resolve
574 swells with $s = 10$ and 40 the spectral grid has 80 directions and 32 frequencies.
575 Larger values of s (i.e., narrower directional spreading) would require higher
576 directional resolution for the model to converge. We use a global integration time
577 step of 200 s, spatial advection time step of 50 s, spectral advection time step of

578 12 s, and minimum source term time step of 5 s. We verified that decreasing the
 579 time stepping or the spatial grid spacing does not significantly change the results
 580 (not shown).

581 All simulations are initialized with the narrow-banded wave spectrum in (A 1).
 582 Waves enter the domain from the left boundary with initial mean direction $\theta =$
 583 0° (propagating from left to right), directional spreading parameter $s = 10$ or
 584 $s = 10$, peak frequency $\sigma_* = 0.61 \text{ rad s}^{-1}$ (peak period of 10.3 s), spectral width
 585 $\delta_\sigma = 0.04$, and $H_{s*} = 1 \text{ m}$. The boundary condition at the left boundary is kept
 586 constant throughout the experiment and each experiment is run until steady state
 587 is reached.

588 As mentioned in §4.1, a control run is conducted in the absence of currents.
 589 Although there is no scattering from the currents, a nonuniform $h_s^{\text{ctrl}} = H_s^{\text{ctrl}} -$
 590 H_{s*} arises, due to the limited domain size in y , which leads to a reduction of
 591 incident wave action from waves arriving from large $|y|$ — an effect that is more
 592 pronounced at large x . As s increases, the action density in the incident spectrum
 593 is more concentrated in the eastward direction, leading to less leakage of wave
 594 action through the top and bottom boundaries and a more spatially uniform h_s^{ctrl} .
 595 This leakage of wave action corresponds to a reduction of 5% in h_s^{ctrl} for $s = 10$,
 596 and 2% for $s = 40$ towards the right-hand side boundary.

597 Appendix C. MA–WW3 mismatch in the scattering region

598 We develop a heuristic correction to MA that we show captures the non-zero h_s
 599 in the scattering region. First, we note that the non-zero h_s in the scattering
 600 region from WW3 appears localized, likely caused by the term proportional to
 601 $\partial_k \mathcal{A}$ in (3.9), as the terms proportional to $\partial_\theta \mathcal{A}$ result in non-local effects. This
 602 observation is confirmed by a WW3 run, which we refer to as WW3⁻, where the
 603 term in $\partial_k \mathcal{A}$ is suppressed in the wave action equation, yielding a more uniform
 604 h_s in the scattering region (see panel (d) in Figure 9). We then recall that in the
 605 MA solution, the insignificance of the $\partial_k \mathcal{A}$ term is due to the approximation of
 606 a single dominant wavenumber in the steps leading to (3.24). We thus return to
 607 the approximation (3.12) of the wave-action transport equation in the scattering
 608 region and relax the approximation of replacing k by k_* . We focus on the θ -
 609 integrated action

$$610 \quad \mathcal{B}(\mathbf{x}, k) = \int \mathcal{A}(\mathbf{x}, \mathbf{k}) d\theta. \quad (\text{C } 1)$$

611 It satisfies

$$612 \quad c(k) \partial_x \mathcal{B} - U_x(\mathbf{x}) k \partial_k \mathcal{B} = 0. \quad (\text{C } 2)$$

613 Noting that $c(k) = g^{1/2} k^{-1/2} / 2$, we solve this equation using the method of
 614 characteristics to find

$$615 \quad \mathcal{B}(\mathbf{x}, k) = \mathcal{B}_* \left(\left(k^{-1/2} - g^{-1/2} U(\mathbf{x}) \right)^{-2} \right). \quad (\text{C } 3)$$

616 The significant wave height is deduced by integration as

$$617 \quad H_s(\mathbf{x}) = \left(\frac{16}{g^{1/2}} \int \mathcal{B}_* \left(\left(k^{-1/2} - g^{-1/2} U(\mathbf{x}) \right)^{-2} \right) k^{3/2} dk \right)^{1/2}. \quad (\text{C } 4)$$

618 We now change the integration variable, taking advantage of the localisation of
 619 $\mathcal{B}_*(k)$ to ignore the corresponding change in the lower limit of integration and

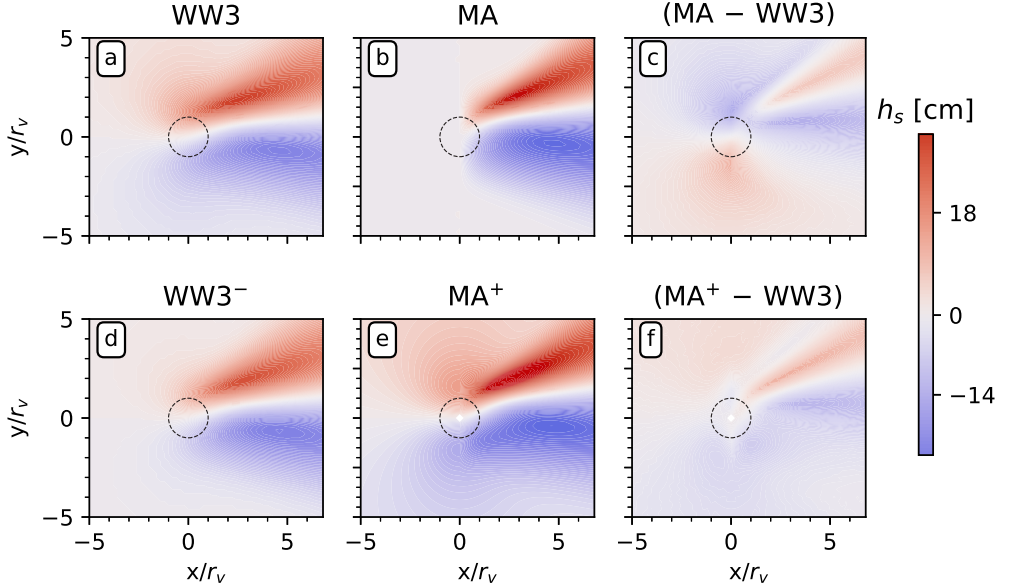


Figure 9: Significant wave height anomaly h_s computed from WW3 (a) and MA (b) as in the main text (same as Figure 3, fourth row); Panel (d) shows h_s from the WW3⁻ run, where the term proportional to $\partial_k \mathcal{A}$ is switched off. Panel (e) shows the MA⁺ solution as in (C 6). Panel (c) shows the difference between (a) and (b), and panel (f) shows the difference between (d) and (e). All panels have the same colorbar.

620 obtain

$$\begin{aligned}
 621 \quad H_s(\mathbf{x}) &= \left(\frac{16}{g^{1/2}} \int \mathcal{B}_*(k) \left(k^{-1/2} + g^{-1/2} U(\mathbf{x}) \right)^{-6} k^{-3/2} dk \right)^{1/2} \\
 622 \quad &= \left(\frac{16}{g^{1/2}} \int \mathcal{B}_*(k) k^{3/2} \left(1 + k^{1/2} g^{-1/2} U(\mathbf{x}) \right)^{-6} dk \right)^{1/2} \\
 623 \quad &= \left(\frac{16}{g^{1/2}} \int \mathcal{B}_*(k) k^{3/2} \left(1 + \frac{U(\mathbf{x})}{2c(k)} \right)^{-6} dk \right)^{1/2} \quad (\text{C } 5)
 \end{aligned}$$

624 At this point, we can approximate $c(k)$ by c_* in the small, $O(\varepsilon)$ term $U(\mathbf{x})/(2c(k))$
 625 and use two binomial expansions to obtain

$$626 \quad H_s(\mathbf{x}) \approx H_{s*} \left(1 - \frac{3U(\mathbf{x})}{2c_*} \right). \quad (\text{C } 6)$$

627 We emphasise the heuristic nature of this approximation (MA⁺) which is formally
 628 no more accurate than the MA approximation $H_s(\mathbf{x}) = H_{s*}$ since it neglects some,
 629 though not all, $O(\delta)$ terms. Nonetheless, it captures most of the significant wave
 630 height anomaly close to the Gaussian vortex, as figure 9 demonstrates under
 631 parameters $s = 40$ and $U_m = 0.8 \text{ m s}^{-1}$.

632 Appendix D. Caustics for the Gaussian vortex

633 In the Gaussian vortex example, we can derive the locations of the caustics in
634 the (x, y) plane analytically. Using expression (4.3) for $\Delta(y)$ and introducing the
635 functions

$$636 \quad w(x, y) \stackrel{\text{def}}{=} -(y - x\theta)^2/r_v^2 \quad (\text{D } 1)$$

637 and

$$638 \quad q(x) \stackrel{\text{def}}{=} -2\pi r_v^4 c_\star^2/(x^2 \kappa^2), \quad (\text{D } 2)$$

639 we can write equations (5.6) defining the caustics as

$$640 \quad \theta - \frac{\kappa}{\sqrt{2\pi r_v c_\star}} e^{w/2} = 0 \quad (\text{D } 3)$$

641 and

$$642 \quad w e^w = q. \quad (\text{D } 4)$$

643 Eq. (D 4) relates w to q , and takes the standard form defining the Lambert W -
644 functions (see Olver 2010, Eq. 4.13.1). This equation has two branches of solutions
645 $w = W_i(q)$, $i = 0, -1$, when $0 < -q < e$ and no solutions when $-q > e$ ($q < 0$ by
646 definition (D 2)). The two branches meet at $q = -e^{-1}$ which corresponds to

$$647 \quad x = x_c \stackrel{\text{def}}{=} \sqrt{2\pi e r_v^2 c_\star}/\kappa. \quad (\text{D } 5)$$

648 Physically, the two branches $w = W_i(q)$ correspond to two caustic lines in the
649 (x, y) plane that emanate from a cusp point with $x = x_c$. The equation of the
650 caustics is found using (D 1) and (D 3) as

$$651 \quad y = \frac{\kappa x e^{W_i(q(x))/2}}{\sqrt{2\pi r_v c_\star}} + \sqrt{-W_i(q(x))} r_v, \quad x \geq x_c. \quad (\text{D } 6)$$

652 The cusp point is at $(x, y) = (x_c, 2r_v)$.

653 The asymptotic form of the caustics for $x \rightarrow \infty$ is readily obtained by noting
654 that $q(x) \rightarrow 0^-$ as $x \rightarrow \infty$ and then that $W_0(q) \rightarrow 0$ and $W_{-1}(q) \sim \ln(-q)$.
655 Thus the $i = 0$ caustic asymptotes to a straight line and the $i = -1$ caustic to
656 $y \sim (2 \ln x)^{1/2}$.

REFERENCES

- 657 ARDHUIN, FABRICE, GILLE, SARAH T, MENEMENLIS, DIMITRIS, ROCHA, CESAR B, RASCLE,
658 NICOLAS, CHAPRON, BERTRAND, GULA, JONATHAN & MOLEMAKER, JEROEN 2017 Small-
659 scale open ocean currents have large effects on wind wave heights. *Journal of Geophysical*
660 *Research: Oceans* **122** (6), 4500–4517.
- 661 COSTE, CHRISTOPHE & LUND, FERNANDO 1999 Scattering of dislocated wave fronts by vertical
662 vorticity and the Aharonov-Bohm effect. ii. dispersive waves. *Physical Review E* **60** (4),
663 4917.
- 664 COSTE, CHRISTOPHE, LUND, FERNANDO & UMEKI, MAKOTO 1999 Scattering of dislocated
665 wave fronts by vertical vorticity and the Aharonov-Bohm effect. i. shallow water. *Physical*
666 *Review E* **60** (4), 4908.
- 667 DYSTHE, KB 2001 Refraction of gravity waves by weak current gradients. *Journal of Fluid*
668 *Mechanics* **442**, 157–159.
- 669 DYSTHE, KRISTIAN, KROGSTAD, HARALD E & MÜLLER, PETER 2008 Oceanic rogue waves.
670 *Annual Review of Fluid Mechanics* **40**, 287–310.
- 671 EWANS, KEVIN C 2002 Directional spreading in ocean swell. In *Ocean Wave Measurement and*
672 *Analysis (2001)*, pp. 517–529.

- 673 GALLET, BASILE & YOUNG, WILLIAM R. 2014 Refraction of swell by surface currents. *Journal*
674 *of Marine Research* **72** (2), 105–126.
- 675 HELLER, EJ, KAPLAN, L & DAHLEN, A 2008 Refraction of a Gaussian seaway. *Journal of*
676 *Geophysical Research: Oceans* **113** (C9).
- 677 HUMBERT, THOMAS, AUMAÎTRE, SÉBASTIEN & GALLET, BASILE 2017 Wave-induced vortex
678 recoil and nonlinear refraction. *Physical Review Fluids* **2** (9), 094701.
- 679 JANSSEN, P 2004 *The Interaction of Ocean Waves and Wind*. Cambridge University Press.
- 680 KENYON, KERN E. 1971 Wave refraction in ocean currents. *Deep-Sea Research* **18**, 1023–1034.
- 681 KIRBY, JAMES T & CHEN, TSUNG-MUH 1989 Surface waves on vertically sheared flows:
682 approximate dispersion relations. *Journal of Geophysical Research: Oceans* **94** (C1),
683 1013–1027.
- 684 KOMEN, GERBRAND J, CAVALERI, LUIGI, DONELAN, MARK, HASSELMANN, KLAUS,
685 HASSELMANN, S. & JANSSEN, P. A. E. M. 1996 *Dynamics and Modelling of Ocean*
686 *Waves*. Cambridge University Press.
- 687 KUIK, AJ, VAN VLEDDER, G PH & HOLTHUIJSEN, LH 1988 A method for the routine analysis
688 of pitch-and-roll buoy wave data. *Journal of Physical Oceanography* **18** (7), 1020–1034.
- 689 LANDAU, LEV DAVIDOVICH & LIFSHITZ, EVGENII MIKHAILOVICH 2013 *Fluid Mechanics: Course*
690 *of Theoretical Physics, Volume 6*. Elsevier.
- 691 LONGUET-HIGGINS, MICHAEL S, CARTWRIGHT, DAVID E & SMITH, ND 1963 Observations of
692 the directional spectrum of sea waves using the motions of a floating buoy. In *Ocean Wave*
693 *Spectra* (ed. Stephan EC), pp. 111–136. Englewood Cliffs, New Jersey: Prentice-Hall.
- 694 MAPP, GEORGE R., WELCH, CHRISTOPHER S. & MUNDAY, JOHN C. 1985 Wave refraction by
695 warm core rings. *Journal of Geophysical Research: Oceans* **90** (C4), 7153–7162, eprint:
696 <https://onlinelibrary.wiley.com/doi/pdf/10.1029/JC090iC04p07153>.
- 697 MCINTYRE, MICHAEL EDGEWORTH 2019 Wave–vortex interactions, remote recoil, the
698 Aharonov–Bohm effect and the Craik–Leibovich equation. *Journal of Fluid Mechanics*
699 **881**, 182–217.
- 700 OLVER, FRANK WJ 2010 *NIST Handbook of Mathematical Functions hardback and CD-ROM*.
701 Cambridge University Press.
- 702 PEREGRINE, D HOWELL 1976 Interaction of water waves and currents. *Advances in Applied*
703 *Mechanics* **16**, 9–117.
- 704 QUILFEN, Y & CHAPRON, B 2019 Ocean surface wave-current signatures from satellite altimeter
705 measurements. *Geophys. Res. Lett.* **46** (1), 253–261.
- 706 ROMERO, LEONEL, HYPOLITE, DELPHINE & MCWILLIAMS, JAMES C 2020 Submesoscale current
707 effects on surface waves. *Ocean Modelling* p. 101662.
- 708 ROMERO, LEONEL, LENAIN, LUC & MELVILLE, W KENDALL 2017 Observations of surface wave–
709 current interaction. *Journal of Physical Oceanography* **47** (3), 615–632.
- 710 VILLAS BOÂS, ANA B., CORNUELLE, BRUCE D., MAZLOFF, MATTHEW R., GILLE, SARAH T. &
711 ARDHUIN, FABRICE 2020 Wave-current interactions at meso and submesoscales: Insights
712 from idealized numerical simulations. *Journal of Physical Oceanography* Submitted.
- 713 VILLAS BÔAS, ANA B. & PIZZO, NICHOLAS 2021 The geometry, kinematics, and dynamics of
714 the two-way coupling between wind, waves, and currents. pp. 18–26. US CLIVAR.
- 715 VILLAS BÔAS, ANA B & YOUNG, WILLIAM R. 2020 Directional diffusion of surface gravity wave
716 action by ocean macroturbulence. *Journal of Fluid Mechanics* **890**, R3.
- 717 VREĆICA, TEODOR, PIZZO, NICK & LENAIN, LUC 2022 Observations of strongly modulated
718 surface wave and wave breaking statistics at a submesoscale front. *Journal of Physical*
719 *Oceanography* **52** (2), 289–304.
- 720 WHITE, BRIAN S. & FORNBERG, BENGT 1998 On the chance of freak waves at sea. *Journal of*
721 *Fluid Mechanics* **355**, 113–138.